Volume 9
Number 37
7 October 2021
Pages 12431–12954

Journal of Materials Chemistry C

Materials for optical, magnetic and electronic devices

rsc.li/materials-c

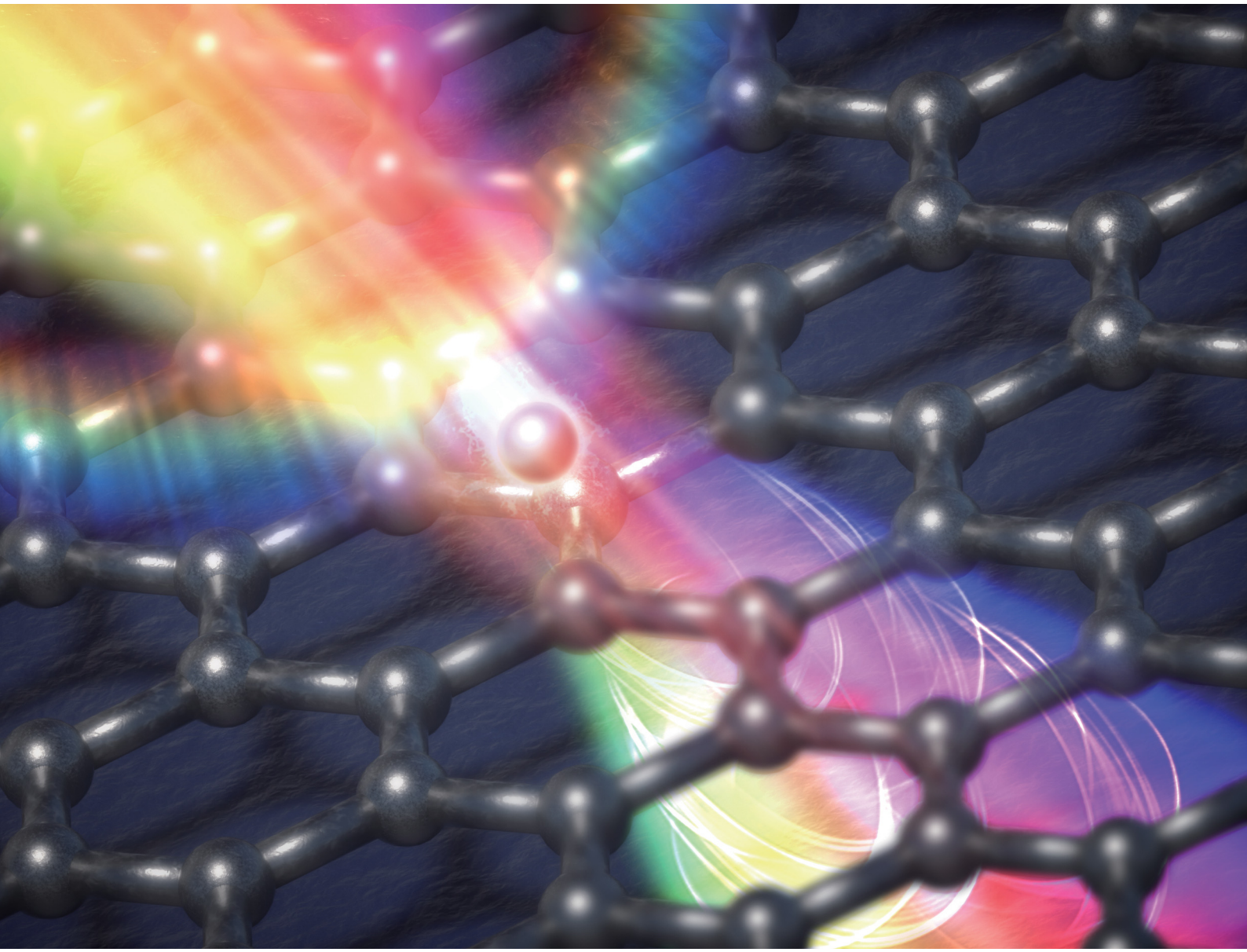

ISSN 2050-7526

ROYAL SOCIETY OF CHEMISTRY

PAPER

Byoung Don Kong *et al.*

Tunable optical property and zero-field splitting of transition metal adatom-graphene quantum dot systems

Journal of Materials Chemistry C

ROYAL SOCIETY OF CHEMISTRY

PAPER

View Article Online
View Journal | View Issue

Check for updates

Cite this: J. Mater. Chem. C, 2021, 9, 12550

Tunable optical property and zero-field splitting of transition metal adatom-graphene quantum dot systems†

Do Hyeon Kim, [a] Adem H. Kulahlioglu, [b] Haewook Han[a] and Byoung Don Kong *[a]

Received 2nd June 2021,
Accepted 9th August 2021

DOI: 10.1039/d1tc02545g

rsc.li/materials-c

Graphene quantum dots (GQDs) with transition metal adatoms were analysed using a first principles approach aimed at finding novel optical materials. The optical properties of the systems that constitute GQDs with a size of 0.4–1.1 nm and five transition metals (Cr, Mo, Pd, Pt, and W) were investigated by time-dependent density functional theory. The HOMO–LUMO gaps, absorption spectra, zero-field splittings, and intersystem-crossing gaps are the main results. Unusual quantum dot size dependencies were found in the energy levels and absorption spectra that stem from extra confinement induced by the transition metal adatoms. Due to the molecular orbital hybridization between GQDs and transition metal adatoms, the major absorption peaks in the visible range could be achieved with a smaller diameter of graphene quantum dots that are relatively free from the influence of deformations. In addition, transition metal-induced magnetic effects were also confirmed by large zero-field splittings, which are negligible in pristine GQDs. The major absorption peaks are located near each red (1.59–1.98 eV), green (2.19–2.38 eV), and blue–violet (2.48–3.26 eV) spectral range, covering the entire visible spectrum, whereas the zero-field splitting mostly covers terahertz regions. These results suggest that the transition metal adatom-GQD systems are strong candidates for optical emission and absorption materials with excellent tunability over a wide spectral range.

Published on 10 August 2021. Downloaded by POSTECH Library on 9/20/2025 5:02:34 PM.

Introduction

Graphene quantum dots (GQDs)[1] are laterally confined graphene structures. Due to the confinement effect, the GQDs show discrete energy levels with gaps. With the advantages inherited from graphene such as bio-compatibility, high solubility, mechanical robustness, and chemical stability, the energy gaps of the GQDs have gained considerable amounts of attention in opto-electronics,[2–6] light emitting diodes (LEDs),[7] bio-imaging[8–10] and sensing[11–15] applications. In particular, GQDs have shown great potential in the display field due to their stable photoluminescence (PL) and superior colour rendering index (CRI).[16] In addition, their low toxicity[17] makes GQDs attractive, unlike the conventional colloidal Group II–VI and IV–VI compound quantum dots that contain Cd and Pb.

The size of a GQD is the primary factor for the PL spectra.[18] As the size of a GQD increases, the quantum confinement effect decreases, and the energy gaps shrink. For this reason, most of the research so far has focused on the energy level dependencies on the GQD sizes and shapes[5,6,19–21] to manage the PL. Ritter and Lyding studied the effects of edge terminations, together with the size variations[17] and showed that GQDs with zigzag edges tend to have smaller bandgaps than those with armchair edges when the diameter is similar.[22] They also found that to manage a pristine GQD optical band edge in the visible range, the required diameter is relatively large, from 1 to 4 nm. The diameter of 4 nm corresponds to 16 × 16 graphene unit cells. At this scale, considering the highly flexible nature of graphene, the energy levels of the GQDs are prone to get influenced by structural deformation such as bending and wrinkles. Indeed, Sk *et al.* reported that the theoretically estimated PL from the GQD with a 1.80 nm diameter was in the red spectral range, whereas the measured emission from the top–down manufactured GQD was in the green spectral range.[6] The primary cause of the mismatch is thought to be the structural disruption of GQD during the fabrication process by the exfoliation from the graphite.[23] This suggests that larger-sized GQDs are required to cover the entire visible spectrum.[6]

Alternative ways to manipulate the HOMO–LUMO gap (HLG) were pursued, including the addition of oxide functional

[a] Department of Electrical Engineering, Pohang University of Science and Technology (POSTECH), Pohang 37673, Korea. E-mail: bdkong@postech.ac.kr
[b] Interdisciplinary Center for Scientific Computing, Ruprecht-Karls University, Heidelberg 69120, Germany

† Electronic supplementary information (ESI) available. See DOI: 10.1039/d1tc02545g

This journal is © The Royal Society of Chemistry 2021

Published on 10 August 2021. Downloaded by POSTECH Library on 9/20/2025 5:02:34 PM.

groups,[24,25] the adsorption of heavy elements (As, Hg,[25] and Pb[16]), the intercalation of potassium–sodium tartrate ($KNaC_4H_4O_6{\cdot}4H_2O$),[26] metalloids (As, B, Ge, Sb, and Si),[27] and fluorination.[28]

In managing the optical spectra of the GQDs, one attractive opportunity resides in GQDs with transition metal (TM) adatoms. Due to the electronegativity, electron transfer from TM to GQD can occur, forming hybrid orbitals. This can reduce the HLG, achieving PL emission in the visible range with a smaller GQD diameter. The additional spin–orbit coupling (SOC) effects, stemming from the orbital hybridization between a TM adatom and a GQD, are also as intriguing as the emission spectra. In this study, various optical properties of TM-GQD complexes are analysed using time-dependent density functional theory (TD-DFT). As a function of the GQD sizes and TM elements, the dependencies of HLG and the dominant absorption peaks are systematically studied. In addition, to provide an integral picture for the TM-GQD complexes, SOC effects, including zero-field splitting (ZFS) and inter-system crossing (ISC) gaps, are also calculated and analysed.

Computational methods

Three different-sized GQDs with five absorbed TM elements (Cr, Mo, Pd, Pt, and W) were investigated (Table 1). A naming convention, of "GQD-*n*," was adopted where *n* is for the total number of atoms. All the dangling bonds of the carbon atoms located at the edges were hydrogen-terminated. As such, the structures studied were designated as GQD-27, -55, and -67, which corresponded to Fig. 1a and b (GQD-27), Fig. 1c and d (GQD-55), and Fig. 1e and f (GQD-67). The same number of atoms occupy a similar area regardless of their shapes, but their optical response may change as the atomic arrangement varies due to the edge effects. For example, 27 carbon atoms can form a long chain, and in this case, the TM is exposed to edge effects more severely. However, the probability of the natural occurrence of such an asymmetrical planar shape seems very low. Accordingly, the structures were constructed so that they had symmetrical shapes, close to a square or a diamond. Both zigzag and armchair terminations were evenly distributed at the horizontal and vertical edges, respectively, in order to exclude the effects from the types of edge terminations.

The five TMs were chosen for the following reason. The different levels of orbital spreading in each metal can alter the optical responses of the TM-GQD complexes even though their atomic valence electron configurations are the same. In order to identify this effect, metals in the same group in the periodic table were selected. The Cr, Mo, and W from Group VI were chosen to study the SOC effects from the TM-GQD orbital hybridization together with the orbital spreading effects. The SOC effects are typically associated with the elements of the half-filled d orbital. As a control, Pd and Pt from Group X with evenly filled orbitals were selected. All the selected metals showed good adhesion to the graphene surfaces experimentally.[29,30]

Table 1 Elemental compositions of TM-GQD complexes. *M* is a transition metal adatom

GQD	Molecular formula
GQD-27	$C_{16}H_{10}M$
GQD-55	$C_{39}H_{15}M$
GQD-67	$C_{48}H_{10}M$

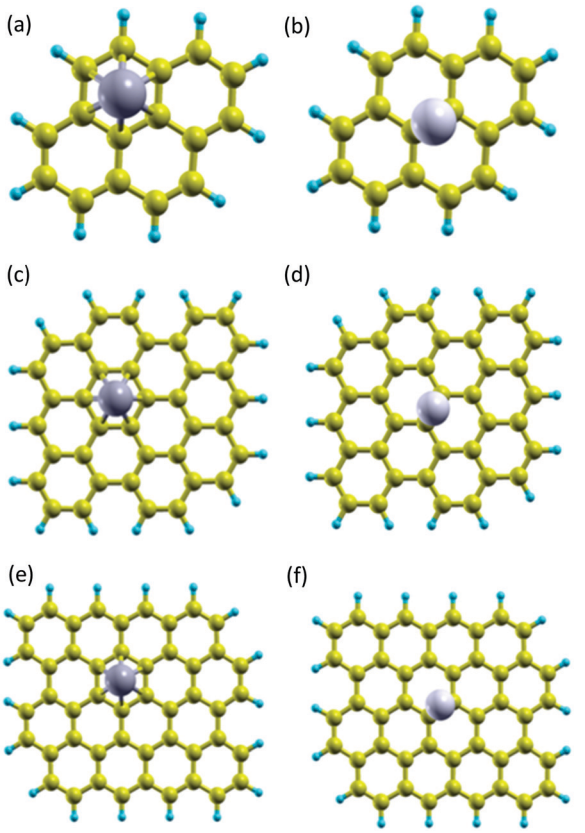

Fig. 1 Hollow sited (a, c and e) and bridge sited (b, d and f) transition metals on GQD surfaces. All the dangling bonds of the carbon atoms at the edges are terminated by hydrogen.

There are multiple possible adsorption sites for a TM atom on the graphene surfaces, but there is a position which is most favoured.[31] As such, the most stable configuration for each TM-GQD complex was considered. Depending on the TM elements, some TM-GQD complexes prefer a hollow site (Fig. 1a), whereas some prefer a bridge site (Fig. 1b). Their preferences are related to the number of valence electrons of a TM. In Group VI, six valence electrons tend to make stable bonds with six carbons at the hollow site. However, Group X TMs are prone to form two bonds to satisfy the octet rule on the bridge site.

The ground state geometry optimizations for each structure were determined by DFT using a Becke-3-Parameter-Lee–Yang–Parr (B3LYP)[32] hybrid functional. The choice of B3LYP was made because it had shown a good performance in estimating HOMO–LUMO gaps in many organic molecules, previously.[33,34] The results obtained by B3LYP and Perdew–Burke–Ernzerhof-0 (PBE0) were compared with the experimental results[35] for Pt-GQDs, and overall, the B3LYP showed a better performance. Ahlrichs def2 family (valence triple-zeta polarization: def2-TZVP)[36] and AuxJ[37] basis sets

Published on 10 August 2021. Downloaded by POSTECH Library on 9/20/2025 5:02:34 PM.

were used for all the atoms. An effective core potential (ECP)[38] approach was adopted for heavy TMs except for Cr. In the geometry optimizations, the following criteria were employed: self-consistent field (SCF) energy change of 5×10^{-6} Ha and gradients of 3×10^{-4} Ha per Bohr.

The SOC-TD-DFT method with Tamm–Dancoff approximation (TDA)[39] was adopted to account for the SOC effects of the excited states. Relativistic effects were considered under zeroth-order regular approximation (ZORA).[35,40] In SOC-TD-DFT,[41] the SOC effects were treated by the usual perturbative approach. Energy differences and transition moments of singlet–singlet, singlet–triplet, and triplet–triplet transitions were computed in the following manner. A T_1. manifold removes its degeneracy and is divided into three sublevels by the SOC or external magnetic field. The SOC can generate a split of a triplet state without an applied field, which is called ZFS. These SOC electric dipole moments are given by:

$$M_j^i = \sum_{n=0}^{\infty} \frac{\langle S_0|\hat{\mu}_j|S_n\rangle\langle S_n|\hat{H}_{SO}|T_1^i\rangle}{E(S_n) - E(T_1)} + \sum_{m=1}^{\infty} \frac{\langle S_0|\hat{H}_{SO}|T_m\rangle\langle T_m|\hat{\mu}_j|T_1^i\rangle}{E(T_m) - E(S_0)}. \quad (1)$$

In eqn 1, M_j^i is mainly proportional to the singlet–singlet transition (S_0–S_n) and the excited singlet-excited triplet transition (S_n–T_1). Starting from this dipole moment, the ZFS can be obtained from the energy difference between the highest and lowest T_1 sublevels.[42]

It is worth mentioning that the adoption of TDA is to handle the hollow sited TM-GQDs (Cr, Mo, W) more accurately. They are open-shell molecules, and it is known that calculating the excited states of open-shell molecules by formal TD-DFT usually undergoes spin-contamination, potentially making the results inaccurate.[43] The same TDA was applied to compare the hollow sited GQDs and the bridge sited GQDs on an equal footing. As a sanity check, a formal TD-DFT calculation was carried out and is provided in the ESI.† The results showed that the TDA is still valid within the TM-GQD systems, and the differences were minimal (Table S2, ESI†).

For calculations up to 40 levels of singlet and triplet excited states were considered using the ORCA DFT package.[44,45] The relativistic Karlsruhe basis set (ZORA-def2-TZVP)[36] was used for carbon and hydrogen atoms, whereas auxiliary basis sets were adopted for elements with a greater atomic number than Kr,[46] and all electron-based SARC[46] for W and Pt, and old-ZORA-TZVP for Mo and Pd.[36] To check the reliability of the calculations and the differences between the approaches, the results of ZORA[47] with the perturbative SOC[41] approach, were compared and only trivial differences were found (Table S1, ESI†).

Results and discussion

Molecular orbital energy states and HLG change

Fig. 2 summarises the molecular orbital (MO) energy levels around the HLGs, and illustrating the clear diameter dependency of the MOs. The HLGs decrease as the size of GQDs gets larger from GQD-27 to GQD-67. One distinct feature, however, that differs in the TM-GQD complexes when compared to the pristine GQDs is the substantially smaller HLGs. The HLGs of the TM-GQD complexes shows 0.5–2.0 eV smaller HLGs than those of the pristine GQDs of the same sizes (Table 2). This means, for example that in the case of the Group VI GQD-27, the HLG of a pristine GQD in the ultraviolet range (3.83 eV) drops to the orange and red region in the visible spectrum range (1.46–2.09 eV) because of the adsorption of a single TM atom on a surface. Whereas all the GQD complexes

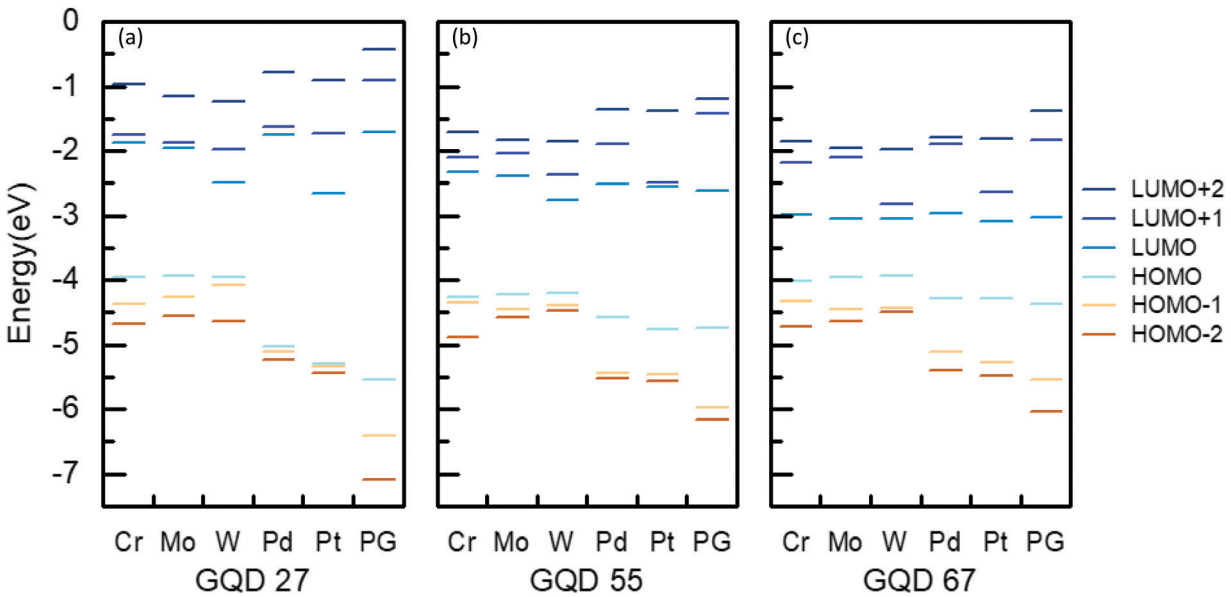

Fig. 2 The energy states of pristine GQDs (PG) and GQDs with different transition metals (Cr, Mo, Pd, Pt, and W). Calculated energy levels of LUMO+2, LUMO+1, LUMO, HOMO, HOMO−1 and HOMO-2 for (a) GQD-27, (b) GQD-35, and (c) GQD-67.

 This journal is © The Royal Society of Chemistry 2021

Published on 10 August 2021. Downloaded by POSTECH Library on 9/20/2025 5:02:34 PM.

Table 2 Summary of HOMO–LUMO energy gaps for all the structures of GQD-27, -55 and -67. ΔE_{size} indicates an HLG decrease from GQD-27 to GQD-55 and from GQD-55 to GQD-67

	Group VI						Group X					
	Cr		Mo		W		Pd		Pt		Pristine	
TM atom species	HLG (eV)	ΔE_{size}	HLG (eV)	ΔE_{size}	HLG (eV)	ΔE_{size}	HLG (eV)	ΔE_{size}	HLG (eV)	ΔE_{size}	HLG (eV)	ΔE_{size}
GQD-27	2.09		1.98		1.46		3.28		2.65		3.83	
		0.16		0.12		0.02		1.23		0.43		1.72
GQD-55	1.93		1.86		1.44		2.05		2.22		2.11	
		0.9		0.95		0.56		0.77		1.05		0.77
GQD-67	1.03		0.91		0.88		1.28		1.17		1.34	

share this trend in common, there are subtle differences depending on the TM species, which will be elaborated on next.

Interestingly, after the adsorption of a TM adatom, the relationship between energy levels and GQD diameters was

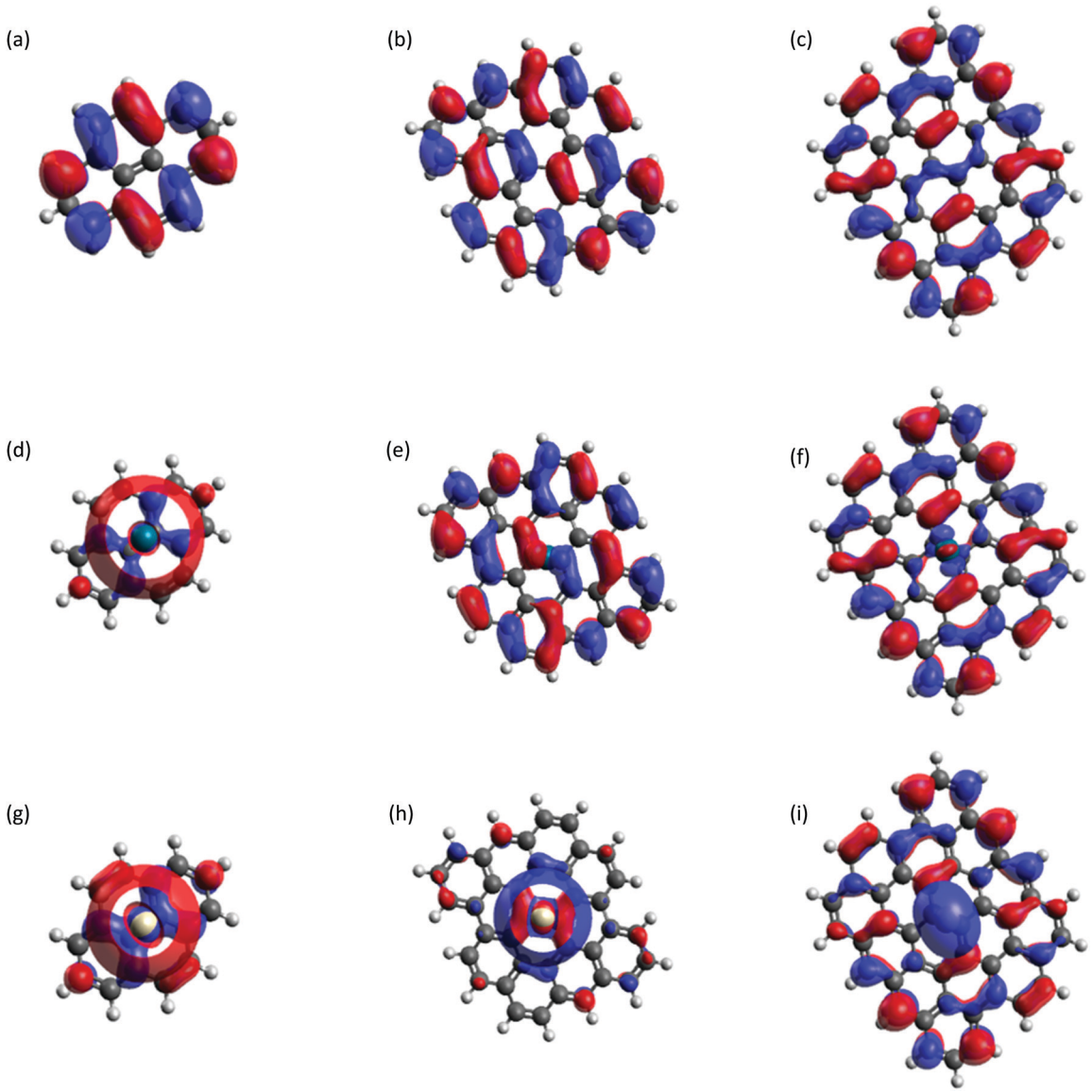

Fig. 3 Iso-surfaces of the LUMO in three different sizes of pristine GQDs and TM-GQDs. (a) pristine GQD-27, (b) pristine GQD-55, (c) pristine GQD-66, (d) Pd-GQD-27, (e) Pd-GQD-55, (f) Pd-GQD-67, (g) Pt-GQD-27, (h) Pt-GQD-55, and (i) Pt-GQD-67. The Pd and Pt are chosen as examples, and the TM-GQDs with Cr, Mo, and W display similar iso-surface shapes to those of the Pt-GQDs. The blue and red lobes indicate the positive and negative parts of orbitals, respectively.

Published on 10 August 2021. Downloaded by POSTECH Library on 9/20/2025 5:02:34 PM.

completely changed. The area expansion from GQD-27 to GQD-55 was about 108%, whereas that from GQD-55 to GQD-67 was 22.2%. As such, in pristine GQDs, ΔE_{size} in HLG from GQD-27 to GQD-55 was more than twice the ΔE_{size} from GQD-55 to GQD-66. However, in TM-GQDs, ΔE_{size} from GQD-55 to GQD-66 was much more pronounced, and the change between GQD-27 to GQD-55 was minimal. The inversely proportional relationship between energy gaps and QD sizes is well-known phenomenon. Yet, this drastic departure from the pristine GQDs can be explained by the TM-GQD orbital hybridization. By the adsorption of a TM adatom, a significant portion of the LUMO of the TM-GQD complexes was formed around the TM adatoms (Fig. 3). As such, the TM atoms cause the spreading of wave functions, making the HLG lower than that of the pristine GQD. However, because the LUMO was confined around the TM adatoms by the hybridization, an adatom provides an extra confinement effect in response to the GQD size. Thus, the energy level shifts caused by the diameter change were diminished. As the GQD diameter becomes larger, however, the energy levels start to become more influenced by the carbon orbitals in a GQD and the size of a GQD. From GQD-55 to GQD-67, only a 22.2% area change caused a 2.4–28 times larger energy shift and HLG change.

One exception from the previous trend is the Pd-GQD complex. The LUMO of Pd-GQD-55 and Pd-GQD-67 (Fig. 3e and f) were significantly different from those of the Pt-GQDs in the same group, and they were rather similar to the LUMO of the pristine GQDs (Fig. 3b and c). Not surprisingly, both Pd- and pristine GQDs showed the same tendency of the HLG energy variation. A Pd adatom on a graphene sheet is known to form an intermediate binding whose strength is between chemisorption and physisorption.[48] This unique charge exchange prevents metal-graphene orbital hybridization being concentrated around the TM, resulting in a LUMO close to that of the pristine GQDs and a similar area dependency. However, the Pd-GQD-27 shows a typical LUMO surface around the TM similar to those of other TM-GQD complexes. This is because the TM on GQD-27 was placed close to the edges due to its small size and this exposed it to the influence of the hydrogen atoms that participate in the charge transfer between Pd and the carbon atoms.

It was found that the TMs with partially filled atomic s and d orbitals showed relatively stronger size dependencies in the HLG characteristics. The calculations performed in this work showed that the size-dependent HLG changes of Cr, Mo, and Pt-GQDs were 0.74, 0.83, and 0.62 eV, respectively, whereas those of W and Pd-GQDs were 0.54 and 0.46 eV, which were slightly smaller (Table 2). This was because the partially filled orbitals of Cr, Mo, and Pt were more reactive compared to the fully filled orbitals of Pd or the partially filled but paired orbitals of W. For Pd and W, fewer electrons were likely to get involved with the carbon-TM interactions.

The energy gaps were also strongly influenced by the TM adsorption sites. In general, hollow sited TMs prefer chemisorption, and bridge sited TMs prefer physisorption. Manadé *et al.* showed that the adsorption energies of hollow sited TMs were larger than those of bridge sited TMs.[31] Thus, the hollow sited TMs (Group VI) tend to bind strongly, forming a hybridized orbital confined around a TM. This reduced the influence from the lateral confinement by the size of the GQDs. With the Group X TMs that adhered to a bridge site, these effects were reduced due to the weak hybridization, resulting in more significant HLG changes as the GQD size increased.

Between TM species in the same group, the energy gap changes were more pronounced as the size of the GQDs became smaller (GQD-27), but eventually, they reached similar HLGs when the GQD size became larger (GQD-67). For example, in Group VI, the HLG difference between Cr-GQD-27 and W-GQD-27 was 0.63 eV, and this difference was reduced to 0.49 eV and 0.15 eV in GQD-55 and GQD-67, respectively. The same tendency can also be seen among the Group X atoms. Because the interaction was confined near the centre of the GQDs around a TM atom, the effects in response to the types of the TM adatom became insignificant as the size of the GQD became larger.

Visible light absorption properties

The absorption spectra of the GQD complexes calculated by TD-DFT are compared in Fig. 4. The energy states and HLGs discussed in the previous section were obtained from ground state calculations, and these energy levels were not necessarily matched to light absorption spectra because light absorption is a process involved with excited states. The TD-DFT is an approach used to evaluate these excited energy states in the frame of DFT, and has been successfully applied to estimate the molecular absorption spectra of many molecular systems.[49] There are multiple peaks in the absorption spectra of TM-GQD complexes calculated by TD-DFT, and the two highest peaks are followed in the following analysis. One common trend that can be found from the calculated spectra is the redshift and intensity increase of the major absorption peaks as the size of the GQDs increased. Most of the major absorption peaks of the TM-GQD-27 complexes (Fig. 4b–e) were distributed near 2.48–3.26 eV which corresponded to the blue–violet region. The Cr-GQD-27 was one exception, and its dominant peaks were located in the red–orange region (1.57 and 2.12 eV). As the size of the GQDs gets larger, the calculated major absorption peaks were observed near the green region (1.98–2.48 eV) with TM-GQD-55s in the near red region (1.59–1.98 eV) with the TM-GQD-67s. The trend was similar for the pristine GQDs (Fig. 4f), but the peaks appeared at higher energy levels. For example, the absorption peaks of the pristine GQD-27 were in the ultraviolet region and do not appear in the graph.

Together with these size-dependent common traits, a different TM adatom altered the light absorption characteristics differently, yet it was more pronounced in smaller TM-GQDs. In Group X, the main peaks of the Pd-GQD-55 were located at 1.90 and 2.58 eV (Fig. 4d), whereas those of Pt were found at 2.04 and 2.50 eV (Fig. 4e). The energy differences between the two TM-GQDs were 0.14 and 0.08 eV, respectively, which was not significant but noticeable. Among the Group VI species, the Cr-GQD-55 displayed the most significant difference compared to the other systems, whereas the differences between Mo and W-GQD-55s were relatively small, only 0.01 and 0.02 eV.

 This journal is © The Royal Society of Chemistry 2021

Published on 10 August 2021. Downloaded by POSTECH Library on 9/20/2025 5:02:34 PM.

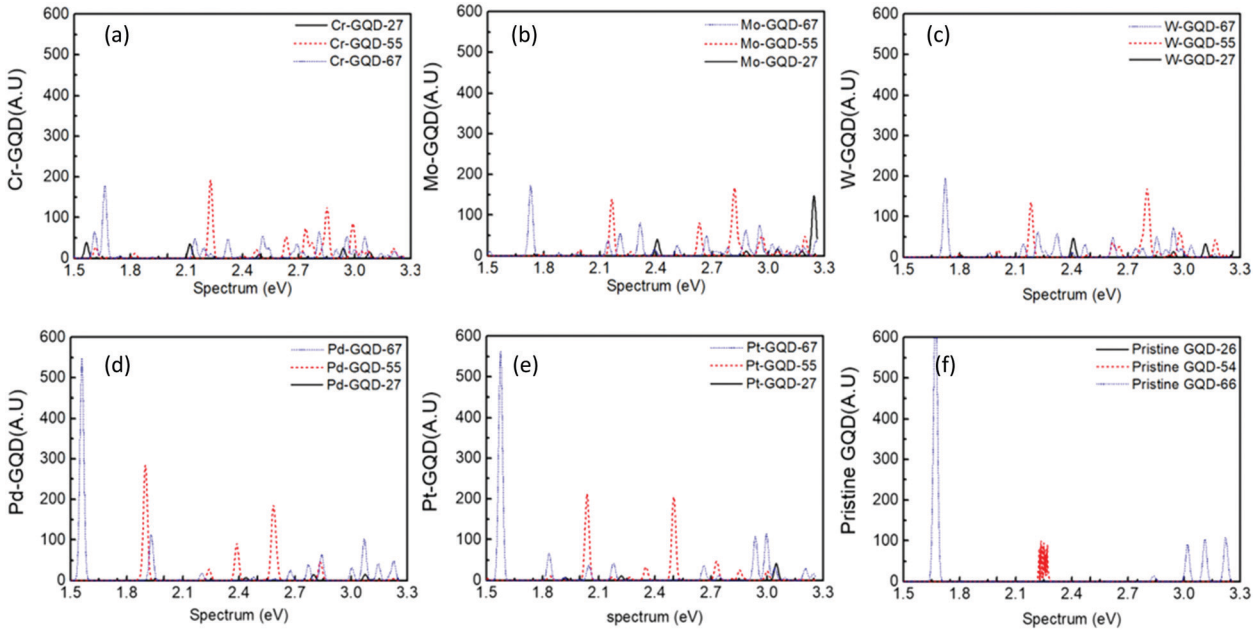

Fig. 4 (a–e) Calculated absorption spectra of TM-GQDs with different TM adatoms. (f) Absorption peaks of pristine GQDs for comparison.

However, as the GQD size reached that of GQD-67, the locations of the absorption peaks became similar, regardless of the TM adatoms, showing that the manipulation of the GQD absorption spectra by the TM adatoms was more effective with a diameter below 1.1 nm.

From the calculated absorption spectra, it was inferred that the light absorption of the TM-GQD complexes could be tuned from red to violet – the entire visible spectrum. In particular, the structures studied have the advantage of making fine-tuned absorption peaks (and naturally emission, too) by controlling two factors: diameters and TM species. The difference to the pristine GQD (Fig. 4e) was that the absorption peaks in the visible range could be obtained with relatively smaller GQD diameters (up to 1.1 nm diameter)[7] that can be immune to the structural deformations.

It was seen, that the trend and the peak energies of the absorption spectra obtained by TD-DFT were slightly different from those of HLGs obtained by ground state calculations. In order to further identify the MOs that were involved with the major absorption peaks, which were not necessarily HOMO and LUMO, the contributions of each orbital transition to major peaks were analysed and the results are summarised in Table 3. Because the large variation was dependent on an adatom, finding a particular trend was very challenging. In the GQD-27 complexes, the largest absorption peaks for each TM-GQD (Cr, Mo, W, Pd, and Pt) came from H-2 → L (95.8% of $\hbar\omega$ = 1.57 eV), H-3 → L (74.8% of $\hbar\omega$ = 3.24 eV), H → L+4 (65.3% of $\hbar\omega$ = 3.11 eV), H-5 → L (65.3% of $\hbar\omega$ = 2.44 eV) and H-1 → L+1 (82.1% of $\hbar\omega$ = 3.05 eV) transitions, respectively, where H and L are HOMO and LUMO, $\pm n$ after H or L is the nth energy level above (+) or below (−). In TM-GQD-55 of Group VI atoms, the transition contributions of the main spectrum were similar to each other. The dominant transitions came from H-2 (or 3) to L+0 (or 1), H-2 → LUMO (68.8% of $\hbar\omega$ = 2.23 eV) for Cr, H-3 → LUMO (72.7% of $\hbar\omega$ = 2.16 eV) for Mo, H-3 → L+1 (76.2% of $\hbar\omega$ = 2.18 eV) for W. In TM-GQD-67, a similar trend in the same group could be noticed, Mo and W are found to be the same (H-1 → L+2), and Pd and Pt are, too (H → L). So, when the size of a GQD was small, the dominant transition peaks displayed a wide variation depending on the TM adatoms, whereas in larger GQDs, the orbital contribution from the graphene side homogenized the transition characteristics.

Zero-field splitting and Inter-system Crossing

Table 4 shows the calculated ZFS values obtained by the ZORA TD-DFT. With the inclusion of the SOC effect, otherwise degenerate first triplet excited states, namely T_{1x}, T_{1y}, and T_{1z}, were split slightly in all cases. The resulting ZFS values were in the THz range (0.8–22 THz), and they were strongly correlated with quantum confinement and the type of TM adatoms used. Roughly speaking, the ZFS tends to be commensurate with the quantum confinement: the ZFS of five different TM-GQD complexes increased as the GQDs shrank. Except for the case of Mo, GQD-55 has a slightly lower ZFS than GQD-67, Cr totally disregards this rule, with GQD-67 having a ZFS multiple times larger than that of GQD-27 and GQD-55.

It is well known that heavier elements display a stronger SOC, and hence they are expected to have a higher ZFS. The Group X complexes satisfied this expectation so that Pt-GQDs have higher ZFS values than Pd-GQDs in all three of the GQD sizes. In fact, the ratio of the ZFS values of Pt-GQDs to those of Pd-GQDs was substantial and increased with the system size. In the Group VI complexes, however, a mixed trend was observed. In the GQDs with a higher quantum confinement, such as GQD-27 and GQD-55, the trend in the ZFS is W-GQD > Mo-GQD > Cr-GQD, which is in parallel with the atomic mass of the TM adatoms. Interestingly, this trend gets reversed in the lowest quantum confinement case, *i.e.*, GQD-67, so that the ZFS values follow the

Published on 10 August 2021. Downloaded by POSTECH Library on 9/20/2025 5:02:34 PM.

Table 3 Energy, coefficients, and contribution of dominant transitions. H and L are for HOMO and LUMO, respectively

	ZORA			
GQD-27	$\hbar\omega$ (eV)	λ (nm)	Dominant transition orbital/transition coefficients (f)	Transition contribution (%)
Cr	1.57	789.70	H-2 → L − 0.98	95.8
	2.12	584.83	H → L+3 0.77	59.8
	2.49	497.93	H-1 → L+3 − 0.82	67.8
	2.94	423.15	H → L+4 − 0.82	67.4
Mo	2.41	514.46	H → L+3 0.81	65.8
	2.88	430.50	H-2 → L+3 − 0.91	83.3
	3.05	406.50	H → L+4 − 0.75	56.3
	3.24	382.67	H-3 → L 0.86	74.8
W	2.41	514.46	H → L+3 0.75	56.0
	2.94	421.71	H-1 → L+4 0.64	41.3
	3.11	398.66	H → L+4 0.80	65.3
Pd	2.44	508.13	H-5 → L − 0.81	65.3
	2.80	442.80	H-1 → L+1 − 0.92	84.1
	3.07	403.86	H-4 → L − 0.78	61.5
Pt	2.22	558.49	H-3 → L − 0.88	77.2
	3.05	406.51	H-1 → L+1 − 0.91	82.1
GQD-55				
Cr	2.23	556.23	H-2 → L − 0.83	68.8
	2.85	434.73	H-1 → L+5 − 0.63	40.4
	2.99	414.80	H-1 → L+7 − 0.70	49.1
Mo	2.16	574.00	H-3 → L − 0.85	72.7
	2.63	471.42	H-3 → L+2 − 0.71	49.9
	2.82	439.66	H-3 → L+3 0.50	25.1
W	2.18	568.21	H-3 → L+1 − 0.87	76.2
	2.81	441.22	H-1 → L+6 0.58	33.5
	2.97	417.46	H-2 → L+5 0.60	36.7
Pd	1.90	652.55	H → L − 0.90	80.6
	2.39	518.76	H-2 → L 0.71	50.6
	2.58	480.56	H-3 → L+1 − 0.64	41.1
Pt	2.04	607.77	H → L+1 − 0.84	71.4
	2.50	495.94	H-2 → L+1 0.72	52.4
Pristine	2.24	551.65	H → L − 0.95	90.7
GQD-67				
Cr	1.60	774.90	H-3 → L+1 0.80	64.5
	1.66	746.89	H-1 → L+4 0.40	15.8
Mo	1.73	716.67	H-1 → L+2 − 0.58	33.8
	2.31	536.73	H-3 → L+3 0.70	48.7
W	1.72	720.84	H-1 → L+2 − 0.57	33.2
	2.94	421.71	H-6 → L 0.47	21.9
Pd	1.56	794.77	H → L − 0.90	81.6
	1.93	642.40	H-3 → L 0.90	81.6
Pt	1.57	789.70	H → L − 0.75	56.0
	3.04	407.84	H-2 → L+2 − 0.79	63.2
Pristine	1.67	742.39	H → L − 0.94	88.2

order of W-GQD < Mo-GQD < Cr-GQD, which is just the opposite of the sequence according to the atomic mass of the TM adatom. This suggests that not only the atomic mass of the TM adatom but also its electronic structure leading to a particular orbital hybridization and carbon-metal charge transfer play significant roles in determining the ZFS. Furthermore, the quantum confinement that significantly impacts on the interaction between TM and the carbon atoms emerges as a useful tool to tune the ZFS.

When focussing on the effect of the TMs, it was evident that the tunability of the ZFS had a strong correlation with the type of binding of the TM atoms and the atomic mass. This mechanism can be analysed using orbital hybridization[50] and graphene-TM charge transfer.[51] Chemisorbed TMs strongly hybridized their d orbital with the π orbital of the pristine graphenes and this can change the electronic structure of the TMs. Therefore, Cr-, Mo-, and W-GQDs were not much affected by the intrinsic properties of the TMs. They showed different ZFS values even though they were in the same group with the same number of unpaired d electrons, and relied on a heavy atomic mass and charge transfer for inducing the SOC. However, physisorbed elements (Pd and Pt) have weak magnetic properties due to their fully filled d orbitals. Hence, some level of charge transfer by the hybridization of their atomic orbitals (π–s orbitals) redistributed their d orbitals, causing ZFS. Probably, this effect was the most pronounced when the GQD size is small, and Pt-GQD-27 showed the largest ZFS, followed by Pt-GQD-55. Then, the ZFS suddenly shrank by 20% to 25% as it reached to Pt-GQD-67. Usually, the ZFS phenomena was closely related to the orbital symmetry breaking. As mentioned, previously, the Group X GQDs with the bridge sited TMs were more symmetrical than the Group VI GQDs with the hollow sited TMs. Yet, the Pt-GQDs showed four to five times larger ZFS values compared with the Group VI GQDs, when the GQD diameter was small. It was suspected that the lateral confinement with the small diameters and orbital hybridization provided extra asymmetry in the Pt-GQDs, and these effects disappeared when the diameter became comparable to the orbital spreading of the elemental Pt. A similar trend can also be observed from the Pd-GQDs.

The calculated ZFS values of Cr- and Mo-GQD-67 did not follow the quantum confinement trend (Table 4), and their ZFS values were higher than those of the smaller GQD complexes. Generally speaking, the TM interaction and binding energy became weaker as the diameter of the GQD increased. Thus, the ZFS energy of the TM-GQD-67 shrank with the other TMs. These unusual ZFS variations with Cr and Mo were thought to be related to the partially occupied atomic orbitals. A large broken rotational symmetry that can be observed in Cr- and Mo-GQD-67 (Fig. 1e) around the axis at the centre of, and vertical to the GQD plane was thought to enhance the magnetization effects from half occupied 4s or 5s orbitals. In the presence of this magnetic field, the degeneracy of the first triplet state was lifted up. Therefore, the ZFS value of Cr- and Mo-GQD-67 surpassed the values of Cr- and Mo-GQD-55.

Table 4 Zero-field splitting for different TMs on different sized GQD complexes. Pristine GQDs do not show zero-field splitting

	Cr		Mo		W		Pd		Pt	
GQD	ΔE (cm^{-1})	Δf (THz)	ΔE (cm^{-1})	Δf (THz)	ΔE (cm^{-1})	Δf (THz)	ΔE (cm^{-1})	Δf (THz)	ΔE (cm^{-1})	Δf (THz)
GQD-27	144.5	4.33	122.9	3.68	207.4	6.22	172.7	5.18	738.8	22.15
GQD-55	76.9	2.30	107.4	3.22	114.8	3.44	5.4	0.16	508.7	15.25
GQD-67	569.7	17.08	116.9	3.50	99.3	2.98	1.1	0.033	28.5	0.80

 This journal is © The Royal Society of Chemistry 2021

Published on 10 August 2021. Downloaded by POSTECH Library on 9/20/2025 5:02:34 PM.

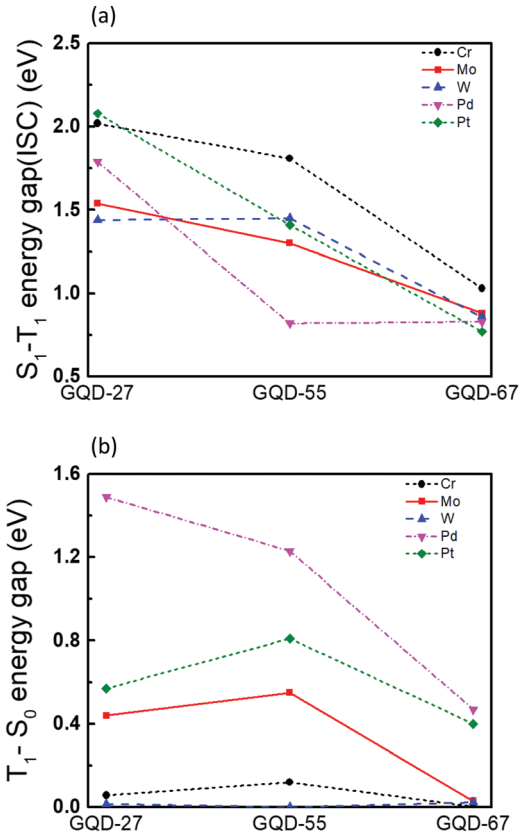

Fig. 5 The calculated energy gap from singlet states and triplet states of the structures, (a) Inter-system crossing gap, and (b) the gap between a singlet ground state and the first excited triplet state.

Together with the ZFS, the ISC gaps, the energy difference between the first singlet excited state (S_1) and the first triplet excited state (T_1), were also of interest because they were essentially phosphorescence characteristics. The calculated ISC gaps of the 15 TM-GQDs are plotted in Fig. 5a. The energy gap between the singlet ground state (S_0) and T_1 ($E_{S_0 \rightarrow T_1}$), which can represent the phosphorescence photon energy, is displayed in Fig. 5b. Both the ICS gaps and $E_{S_0 \rightarrow T_1}$ decreased as the GQD size increased. This general trend was mainly due to the reduction of the HLGs, which essentially corresponded to $E_{S_0 \rightarrow S_1}$ because E_{T_1} is relative to E_{S_0} and E_{S_0} in general. However, depending on the TM adatoms, some show unusual trends. For example, a sudden increase of E_{T_1} can be found with Pt and Mo at TM-GQD-55, and the ISC gap of the Pd-GQD decreased abruptly at GQD-55. These all show a strong correlation with the magnetic properties of the TM-GQDs so that Pt- and Mo-GQDs had the minimum variation of ZFS as the size increased, and the Pd-GQDs showed the smallest ZFS values. Also, similar to the previously discussion about other optical properties, when the diameters of the GQDs became greater than that of the TM-GQD-67, the orbital contribution from the graphene side started to play a dominant role, resulting in similar energy levels regardless of the TM adatoms. As such, the ISC gaps became almost the same in all the TM-GQDs, whereas the $E_{S_0 \rightarrow T_1}$ converged into values which were dependent on the number of d electrons of a TM.

The calculated ZFS and ISC gaps demonstrated that quantum confinement can impact on both the fluorescence and phosphorescence spectra. Moreover, combined with the absorption spectra discussed in the previous section, the ZFS and ISC also illustrate that a good manoeuvrability of the optical characteristics can be obtained in a wide spectral range, from THz to visible, with the TM-GQD systems by a judicious choice of the TM adatom and the size of GQDs.

Conclusions

The excited energy levels and the absorption properties of TM-GQDs were investigated, with the aim of consolidating the knowledge of the optical tunability of the TM-GQD systems. First, the HLG and frontier orbital states of these structures were calculated, and then the size and TM adatom dependencies were obtained. The calculated HLGs show unusual trends, such as non-linear proportionality with the size of the GQDs. For example, the energy differences between GQD-55 and GQD-67 are much more significant than those between GQD-27 and GQD-55, and it was shown that these results can be understood based on the TM-graphene charge transfer and the extra-confinement provided by the TM adatoms. The analysis of the visible absorption and the peak spectral distributions revealed that the major absorption peaks of the TM-GQDs are located in the red region (1.59–1.98 eV on GQD-67), the green region (2.19–2.38 eV on GQD-55), and the blue-violet region (2.48–3.26 eV on GQD-27), indicating that the systems studied can cover the entire visible range with fine optical tunability.

The ZFS and ISC were calculated by analysing the SOC-induced, otherwise degenerate, first excited triplet substrates. The results suggest that the TM-GQDs also offer great potential for tunability in the THz range by manipulating the GQD sizes and the TM adatoms. For this purpose, Pd and Pt in Group X induce larger SOC effects than the Group VI TMs due to their adhesion site, and they provide a prompt change in the phosphorescence properties as a function of the GQD size.

This study is not limited to isolated GQDs but can also be applied to many similar systems. For example, graphene oxides with 1–4 nm diameter pristine graphene patches are also expected to show similar light absorption properties when the surface accommodates TM adatoms. Together with the tunable optical sources in the visible and THz ranges, these results can provide a systematic understanding of two significant optical absorption properties, fluorescence and phosphorescence, and SOC-induced ZFS in various TM decorated graphene systems. This study illustrates the potential of the TM-GQDs for use in stable imaging and THz radiation sources without concerns about deformation. The calculated data can provide specific GQD synthesis conditions, including the diameter and the species of adatom for the target frequencies.

Conflicts of interest

There are no conflicts to declare.

Published on 10 August 2021. Downloaded by POSTECH Library on 9/20/2025 5:02:34 PM.

Acknowledgements

This work was supported in part by the BK21 Plus program, Samsung Research Funding and Incubation Centre of Samsung Electronics, Korea (SFRC-IT1802-01), and the National Research Foundation of Korea (NRF) grant funded by the Korean Government (MSIT) (No. 2021M3F3A2A03017770).

Notes and references

1 J. Peng, W. Gao, B. K. Gupta, Z. Liu, R. Romero-Aburto, L. Ge, L. Song, L. B. Alemany, X. Zhan, G. Gao, S. A. Vithayathil, B. A. Kaipparettu, A. A. Marti, T. Hayashi, J. J. Zhu and P. M. Ajayan, *Nano Lett.*, 2012, **12**, 844–849.
2 D. Raeyani, S. Shojaei and S. Ahmadikandjani, *Mater. Res. Express*, 2020, **7**, 015608.
3 A. Bayat and E. Saievar-Iranizad, *J. Lumin.*, 2017, **192**, 180–183.
4 G. Bharathi, D. Nataraj, S. Premkumar, M. Sowmiya, K. Senthilkumar, T. D. Thangadurai, O. Y. Khyzhun, M. Gupta, D. Phase, N. Patra, S. N. Jha and D. Bhattacharyya, *Sci. Rep.*, 2017, **7**, 1–17.
5 S. Chopra and L. Maidich, *RSC Adv.*, 2014, **4**, 50606–50613.
6 M. A. Sk, A. Ananthanarayanan, L. Huang, K. H. Lim and P. Chen, *J. Mater. Chem. C*, 2014, **2**, 6954–6960.
7 H. Yoon, H. S. Kim, J. Kim, M. Park, B. Kim, S. Lee, K. Kang, S. Yoo and S. Jeon, *ACS Appl. Nano Mater.*, 2020, **3**, 6469–6477.
8 M. Zhang, L. Bai, W. Shang, W. Xie, H. Ma, Y. Fu, D. Fang, H. Sun, L. Fan, M. Han, C. Liu and S. Yang, *J. Mater. Chem.*, 2012, **22**, 7461.
9 X. Zhu, Y. Liu, P. Li, Z. Nie and J. Li, *Analyst*, 2016, **141**, 4541–4553.
10 Z. Su, H. Shen, H. Wang, J. Wang, J. Li, G. U. Nienhaus, L. Shang and G. Wei, *Adv. Funct. Mater.*, 2015, **25**, 5472–5478.
11 X. Liu, W. Na, H. Liu and X. Su, *Biosens. Bioelectron.*, 2017, **98**, 222–226.
12 Y. R. Kumar, K. Deshmukh, K. K. Sadasivuni and S. K. K. Pasha, *RSC Adv.*, 2020, **10**, 23861–23898.
13 I. Shtepliuk, N. M. Caffrey, T. Iakimov, V. Khranovskyy, I. A. Abrikosov and R. Yakimova, *Sci. Rep.*, 2017, **7**, 1–17.
14 Y. Dong, C. Chen, X. Zheng, L. Gao, Z. Cui, H. Yang, C. Guo, Y. Chi and C. M. Li, *J. Mater. Chem.*, 2012, **22**, 8764–8766.
15 I. Shtepliuk and R. Yakimova, *Materials*, 2018, **11**, 1–14.
16 L. Wang, Y. Wang, T. Xu, H. Liao, C. Yao, Y. Liu, Z. Li, Z. Chen, D. Pan, L. Sun and M. Wu, *Nat. Commun.*, 2014, **5**, 1–9.
17 X. Hai, J. Feng, X. Chen and J. Wang, *J. Mater. Chem. B*, 2018, **6**, 3219–3234.
18 R. Q. Zhang, E. Bertran and S. T. Lee, *Diamond Relat. Mater.*, 1998, **7**, 1663–1668.
19 S. S. R. K. C. Yamijala, M. Mukhopadhyay and S. K. Pati, *J. Phys. Chem. C*, 2015, **119**, 12079–12087.
20 R. Esteban-Puyuelo, R. K. Sonkar, B. Pujari, O. Grånäs and B. Sanyal, *Phys. Chem. Chem. Phys.*, 2020, **22**, 8212–8218.
21 Z. Ji, E. Dervishi, S. K. Doorn and M. Sykora, *J. Phys. Chem. Lett.*, 2019, **10**, 953–959.
22 K. A. Ritter and J. W. Lyding, *Nat. Mater.*, 2009, **8**, 235–242.
23 S. J. Bradley, R. Kroon, G. Laufersky, M. Röding, R. V. Goreham, T. Gschneidtner, K. Schroeder, K. Moth-Poulsen, M. Andersson and T. Nann, *Microchim. Acta*, 2017, **184**, 871–878.
24 Y. Li, H. Shu, X. Niu and J. Wang, *J. Phys. Chem. C*, 2015, **119**, 24950–24957.
25 S. Chen, N. Ullah, T. Wang and R. Zhang, *J. Mater. Chem. C*, 2018, **6**, 6875–6883.
26 S. H. Song, M. H. Jang, J. Chung, S. H. Jin, B. H. Kim, S. H. Hur, S. Yoo, Y. H. Cho and S. Jeon, *Adv. Opt. Mater.*, 2014, **2**, 1016–1023.
27 Y. Shuai, M. Rafique, M. Moazam Baloch, M. Ali Tunio and I. Ahmed, *Chem. Phys.*, 2020, **536**, 110828.
28 P. Gong, J. Wang, K. Hou, Z. Yang, Z. Wang, Z. Liu, X. Han and S. Yang, *Carbon*, 2017, **112**, 63–71.
29 Q. Pang, L. Li, C. L. Zhang, X. M. Wei and Y. L. Song, *Mater. Chem. Phys.*, 2015, **160**, 96–104.
30 K. Nakada and A. Ishii, *Solid State Commun.*, 2011, **151**, 13–16.
31 M. Manadé, F. Viñes and F. Illas, *Carbon*, 2015, **95**, 525–534.
32 A. D. Becke, *J. Chem. Phys.*, 1988, **88**, 2547–2553.
33 L. Kronik, T. Stein, S. Refaely-Abramson and R. Baer, *J. Chem. Theory Comput.*, 2012, **8**, 1515–1531.
34 M. Zhao, F. Yang, Y. Xue, D. Xiao and Y. Guo, *Chem. Phys. Chem.*, 2014, **15**, 950–957.
35 M. A. L. Marques, J. Vidal, M. J. T. Oliveira, L. Reining and S. Botti, *Phys. Rev. B: Condens. Matter Mater. Phys.*, 2011, **83**, 1–5.
36 F. Weigend and R. Ahlrichs, *Phys. Chem. Chem. Phys.*, 2005, **7**, 3297–3305.
37 F. Weigend, *Phys. Chem. Chem. Phys.*, 2006, **8**, 1057–1065.
38 D. Andrae, U. Häußermann, M. Dolg, H. Stoll and H. Preuß, *Theor. Chim. Acta*, 1990, **77**, 123–141.
39 S. Grimme, *J. Chem. Phys.*, 2013, **138**, 244104.
40 J. M. Younker and K. D. Dobbs, *J. Phys. Chem. C*, 2013, **117**, 25714–25723.
41 B. De Souza, G. Farias, F. Neese and R. Izsák, *J. Chem. Theory Comput.*, 2019, **15**, 1896–1904.
42 K. Mori, T. P. M. Goumans, E. Van Lenthe and F. Wang, *Phys. Chem. Chem. Phys.*, 2014, **16**, 14523–14530.
43 Z. Li, W. Liu, Y. Zhang and B. Suo, *J. Chem. Phys.*, 2011, **134**, 134101.
44 F. Neese, *Wiley Interdiscip. Rev.: Comput. Mol. Sci.*, 2012, **2**, 73–78.
45 F. Neese, *Wiley Interdiscip. Rev.: Comput. Mol. Sci.*, 2018, **8**, 4–9.
46 D. A. Pantazis, X. Y. Chen, C. R. Landis and F. Neese, *J. Chem. Theory Comput.*, 2008, **4**, 908–919.
47 C. Van Wüllen, *J. Chem. Phys.*, 1998, **109**, 392–399.
48 R. Mao, B. D. Kong, C. Gong, S. Xu, T. Jayasekera, K. Cho and K. W. Kim, *Phys. Rev. B: Condens. Matter Mater. Phys.*, 2013, **87**, 1–7.
49 A. D. Laurent and D. Jacquemin, *Int. J. Quantum Chem.*, 2013, **113**, 2019–2039.
50 C. Gong, G. Lee, B. Shan, E. M. Vogel, R. M. Wallace and K. Cho, *J. Appl. Phys.*, 2010, **108**, 1233711.
51 G. Giovannetti, P. A. Khomyakov, G. Brocks, V. M. Karpan, J. Van Den Brink and P. J. Kelly, *Phys. Rev. Lett.*, 2008, **101**, 4–7.

 This journal is © The Royal Society of Chemistry 2021